Journal of Materials Chemistry A

# Optimization of Nonatitanate Electrodes for Sodium-Ion Batteries

| | |
|---|---|
| Journal: | *Journal of Materials Chemistry A* |
| Manuscript ID | TA-ART-08-2020-007561.R1 |
| Article Type: | Paper |
| Date Submitted by the Author: | 03-Sep-2020 |
| Complete List of Authors: | Alvarado, Judith; Lawrence Berkeley National Laboratory, Energy Storage and Distributed Resources Division<br>Barim, Gözde; Lawrence Berkeley National Laboratory, Energy Storage & Distributed Resources<br>Quilty, Calvin; Stony Brook University, Department of Chemistry<br>Yi, Eongyu; Lawrence Berkeley National Laboratory, Energy Storage and Distributed Resources Division<br>Takeuchi, Kenneth; Stony Brook University, Chemistry<br>Takeuchi, Esther; Stony Brook University, Materials Science and Engineering<br>Marschilok, Amy; Stony Brook University, Materials Science and Engineering<br>Doeff, Marca; Lawrence Berkeley National Laboratory, |
| | |

# Optimization of Nonatitanate Electrodes for Sodium-Ion Batteries

Judith Alvarado[1,§], Gözde Barim[1,§], Calvin D. Quilty[2], Eongyu Yi[1], Kenneth J. Takeuchi[2,3], Esther S. Takeuchi[2,3,4], Amy C. Marschilok[2,3,4], Marca M. Doeff[1,*]

1. Energy Storage & Distributed Resources Division, Lawrence Berkeley National Laboratory, Berkeley, CA 94720.
2. Department of Chemistry, Stony Brook University, Stony Brook, NY 11794.
3. Department of Materials Science and Chemical Engineering, Stony Brook University, Stony Brook, NY 11794.
4. Energy and Photon Sciences Directorate, Brookhaven National Laboratory, Upton, NY 11973.

## Abstract

$NaTi_3O_6(OH)\cdot 2H_2O$, also known as "sodium nonatitanate" (NNT) can undergo reversible sodium (de)insertion at low potentials centered around 0.3 V. The low average insertion potential and high theoretical capacity (~200 mAh/g based on site considerations) suggest that it can be a promising high energy density anode material for sodium-ion batteries. However, its low practical capacity, poor capacity retention, and low initial Columbic efficiency require further material and electrode optimization. Herein, the optimization of the material properties of NNT as well as electrode engineering were used to improve these aspects of electrochemical performance. Characterization tools including pair distribution function analysis, synchrotron X-ray diffraction, and soft and hard X-ray absorption spectroscopy were utilized to probe details of the crystal and electronic structure. Upon drying, rearrangement of the sodium ions in the interlayer space and formation of O-Na-O bridges occur. Hard and soft X-ray absorption spectroscopy show that charge transfer occurs upon discharge of the material in sodium half-cells, consistent with a reversible reductive intercalation mechanism. The best-performing electrodes were dehydrated at 500°C, and the highest initial capacities of about 200 mAh/g were obtained when a CMC binder was used and NNT was carbon-coated. Wrapping NNT with only 1 wt. % graphene also resulted in improved performance.

## Introduction

The development of sodium-ion batteries, especially for large-scale grid storage applications, has been driven by three factors: 1) lithium supply chain issues; 2) lithium cost; and, 3) abundance of lithium. Sodium-ion batteries can be used as drop-in replacements for lithium-ion batteries owing to the similarities of the two technologies. The development of sodium-ion batteries has reached an advanced level and, they are possibly the closest to commercialization among all the "Beyond Lithium Ion" systems.

Hard carbons and alloy materials have been widely studied as anode materials for sodium-ion batteries.[1-4] Although hard carbons are the most used anode materials for sodium-ion batteries, their extremely low insertion potentials can cause potential safety issues due to sodium plating.[5,6] Na/Sn or Na/P alloy systems have also been considered as anode alternatives.[7-9] However, alloys

suffer from large volume changes during electrochemical cycling, which causes significant mechanical and chemical instabilities that negatively affects the energy density over time.[10-11] Sodium titanates are also promising anodes due to the layered or tunnel structures that reversibly intercalate sodium ions at low potentials.[12-14] Recently, our group has described several types of intercalation anodes based on sodium titanates with low potentials and high capacities.[15-19] These materials are denser than carbon and have smaller volume changes than the alloys, therefore, full utilization of sodium titanates in a sodium-ion battery may lead to higher energy density, better cycling stability, and improved safety over the options listed above.

One of these, $NaTi_3O_6(OH)\cdot 2H_2O$ (NNT) has a layered structure consisting of corner- and edge-shared $TiO_6$ octahedra forming stepped layers of $Ti_6O_{14}$, with exchangeable sodium ions and water molecules residing between the layers. The theoretical capacity based on site considerations is about 200 mAh/g, assuming that intercalated sodium can replace water between the titanate layers. Both the as-synthesized and the dehydrated NNT are electrochemically active as reported previously.[16] The average voltage of 0.3 V vs $Na/Na^+$ with a gradually sloping voltage profile suggests a single-phase solid-solution type of insertion mechanism. When NNT is dehydrated at 600 ˚C, it displays good cycling reversibility. Conversely, the as-synthesized NNT in the original report showed poor cycling performance due to electrode degradation. The structure of the dried NNT is stabilized by the formation of linking bonds, which leads to better cycling performance, and the 125 mAh/g second cycle capacity of the dehydrated NNT was retained after 20 cycles.[15] Both materials exhibit very high first cycle Coulombic inefficiencies due to side reactions (*e.g.* reduction of the electrolyte solution to form an solid-electrolyte interphase (SEI) as well as irreversible intercalation of sodium ions into carbon additives) at the very low potentials. De-insertion of interlayer water and its reduction also contribute to first cycle inefficiencies in the case of the as-synthesized material. Removal of the two interlayer water molecules, whether electrochemically or through a dehydration step, allows access to two additional sites per formula unit. However, in the previous reports, less than the expected capacity was obtained, based on these site considerations. This observation prompted the current work.

Here, we report optimization of the electrochemical performance of sodium nonatitanate by material and electrode engineering. Structural properties of the as-synthesized and dehydrated NNT were characterized by synchrotron X-ray diffraction (XRD), electron microscopy, and pair distribution function (PDF) analyses. The impact of dehydration temperature on the crystal structure was explored *via* temperature-controlled XRD, which led to further electrochemical improvements. Various binders and carbon-coating procedures were implemented to increase the initial Coulombic efficiency and cycling reversibility of dehydrated NNT. Hard and soft X-ray Absorption Spectroscopy (XAS) further elucidated the redox reaction mechanism behavior of NNT as a function of depth of (dis)charge.

## Experimental

### Synthesis:

$NaTi_3O_6(OH) \cdot 2H_2O$ (NNT) was synthesized hydrothermally as previously described in the literature.[16] 5 mL of deionized water and 7.8 g of sodium hydroxide solution (50 wt%, Sigma-Aldrich) were mixed together. 6.25 g of titanium isopropoxide (97%, Sigma-Aldrich) was then added dropwise while stirring. The resulting white gel was stirred for half an hour to obtain a homogeneous mixture and transferred to a 42 mL volume pressure vessel with a Teflon lining. The mixture was then heated at 200 ˚C for 24 h. The resulting white substance was filtered, washed, and dried at room temperature in air. Several as-made samples were dried at various temperatures ranging from 300-800 ˚C for 2 h.

Carbon coated NNT was prepared using sucrose pyrolysis following the procedure outlined by Lee and coworkers.[20] The subsequent NNT-sucrose material was carbonized and dehydrated at 500 ˚C or 600 ˚C in an Argon filled tube furnace for 2 h.

Graphene-wrapped NNT was synthesized by a similar hydrothermal approach. 2 mL of graphene oxide (1 wt%, Graphanea), 3 mL of deionized water and 7.8 g of sodium hydroxide solution (50 wt%, Sigma-Aldrich) were mixed together and 6.25 g of titanium isopropoxide (97%, Sigma-Aldrich) was added dropwise while stirring. The resulting gray gel were stirred for half an hour to obtain a homogeneous mixture and transferred to a 42 mL volume pressure vessel with a Teflon lining. The mixture was heated at 200 ˚C for 24 h. The resulting gray substance was filtered, washed, and dried at room temperature in air.

### Characterization:

Scanning electron microscopy (SEM) was performed on a JEOL JSM-7000F with a Thermo Scientific energy dispersive X-ray spectroscopy (EDS) detector. Thermogravimetric analysis (TGA) under nitrogen using a heating rate of 5 °C/minute was carried out on a TA Instruments Q5500 TGA-MS instrument.

Temperature-controlled XRD analysis was done using a Panalytical X'Pert Pro diffractometer with monochromatized Cu Kα radiation equipped with an Anton Parr HTK 1200 hot stage. Scans were collected between 15 and 75° (2θ) at a rate of 0.0001°/s and a step size of 0.022°. A ramp rate of 5 ˚C/minute was used and the temperature was held for one hour before acquiring the XRD patterns.

**Electrochemical Testing:**

The electrochemical properties of the compounds were evaluated in two-electrode 2032-coin cells containing metallic sodium as the counter electrode. Sodium disks were made by extruding dry sodium sticks (Sigma-Aldrich) into thin foils and cutting to size. Composite working electrodes were prepared by making a slurry of 70 wt% of sodium titanate, 25 wt% acetylene black (Denka, 50% compressed), and 5 wt% polyvinylidene difluoride (PVDF) (>99.5%, Aldrich) in N-methyl-2-pyrrolidinone (NMP) or 5 wt% carboxymethyl cellulose (CMC, 250,000 MW) binder solution. The slurry was then cast onto carbon coated aluminum foil. The electrodes were dried first in air and then under vacuum at 120 ˚C for 12 h before being cut to size and weighed. The typical loading and thickness were 3-4 mg $cm^{-2}$ and 60 μm, respectively. The electrolyte used for sodium cells was a solution of 1 M $NaPF_6$ (Sigma-Aldrich) in ethylene carbonate–dimethylene carbonate (EC : DMC) 3 : 7 mol (BASF) mixed in-house. Galvanostatic cycling experiments were carried out with a Bio-logic VMP3 potentiostat/galvanostat at room temperature. The cyclic voltammetry (CV) was studied on EC-Lab software between 0.1−2.0 V with a scan rate of 0.5 mV/s.

**Synchrotron Analysis:**

The NNT electrodes were cycled to a specific state of charge and disassembled in an argon-filled glovebox. The electrodes were subsequently washed with dimethyl carbonate to remove salt residue. The dried and washed electrodes were sealed with kapton tape in an argon-filled glovebox and placed in aluminum pouches for transfer. All measurements were carried out in both transmission and fluorescence modes at beamline 4-3 at Stanford Synchrotron Radiation Lightsource (SSRL). Calibration was applied to all spectra using the first inflection point of the corresponding Ti metal foil. XANES data were analyzed using Athena software.

Samples for the ex-situ soft XAS studies were prepared similarly to those for the hard XAS experiments. The NNT cycled electrodes were mounted onto aluminum sample holders with double-sided carbon tape in an argon-filled glove box, placed into a sealed jar contained within another jar and transferred to a glove bag purged with argon connected to the XAS load-lock chamber. Measurements were conducted on beamline 10-1 at SSRL, using a 31-pole wiggler and a spherical grating monochromator with 20 mm entrance and exit slits, a 0.2 eV energy resolution and a 1 $mm^2$ beam spot. Data were collected at room temperature under ultrahigh vacuum ($10^{-9}$ Torr) using the total electron yield (TEY) and fluorescence yield (FY) mode detectors.

X-ray diffraction data was collected on beamline 28-ID-1 at the National Synchrotron Light Source-II in Brookhaven National Laboratory. The X-ray wavelength was calibrated to 0.1668 Å using a $LaB_6$ standard and a 16-inch amorphous silicon 2D detector with a CsI scintillator was employed. Samples were carefully packed between two pieces of polyimide Kapton tape and data were collected on an empty double layer of Kapton tape and subtracted from the experimental XRD patterns. 2D data calibration and integration into 1D patterns was performed in Fit2D. XRD

data fitting was accomplished by the Rietveld refinement method and performed in GSAS-II.[21] xPDFSuite was used to transform the XRD data into the corresponding pair distribution function (PDF); the $Q_{min}$ and $Q_{max}$ were 0.1 and 12.7 $Å^{-1}$ respectively and an $r_{poly}$ of 1.02 Å was used.[22] $Q_{damp}$ and $Q_{broad}$ parameters of 0.04 and 0.014 $Å^{-1}$ respectively were determined through fitting the PDF of the $LaB_6$ standard in PDFGUI.[23] PDFGUI was also used for fitting the PDF data.

## Results and Discussion

### *NNT structural analysis*

To determine the structure of the as-made and anhydrous sodium nonatitanate (NNT) dried at 600°C, synchrotron XRD data was collected on the materials and is shown in **Fig. S1**. Both materials are layered and nanocrystalline, as evidenced by the significant peak broadening and the intense peak below 2θ=2°, which suggests large interlayer spacings throughout the structures. In the case of the anhydrous NNT, this peak is shifted to a higher angle indicating a contraction of 8.5 to 7.3 Å consistent with the removal of water molecules from the interlayer space upon high temperature dehydration. To gain more quantitative structural information, Rietveld refinements were performed on patterns collected on both materials (**Fig. 1**).

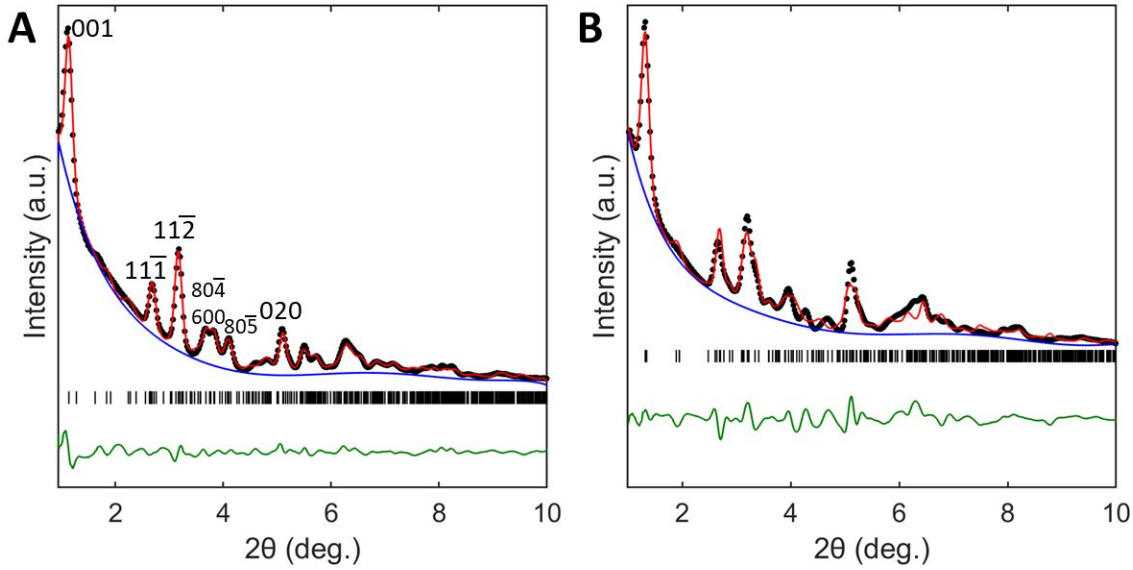


**Fig. 1.** Rietveld refinements of XRD patterns of **(a)** NNT as-prepared (%$R_{wp}$=2.49) and **(b)** anhydrous NNT (%$R_{wp}$=4.63). The black points represent the data, the red line represents the fit, the blue is the background, and the green is the difference between the experimental data and the fit. The black lines represent the expected reflections from the structural model.[24]

The as-made material was identified through refinement as $NaTi_3O_6OH{\cdot}xH_2O$ (space group = *C2/m*, *a*=21.555 Å, *b*=3.7583 Å, *c*=11.926 Å, and β=136.14°) as shown in **Fig. S2a** (the

refinement results are shown in **Tables S1** and **S2)**.[24] The unit cell of the as-prepared NNT material agrees well with that expected for $NaTi_3O_6OH{\cdot}xH_2O$ and is composed of sheet-like crystallites with a thickness of 22 nm along the layering [(001)] axis. The material is also significantly hydrated with a formula of $NaTi_3O_6OH{\cdot}2H_2O$, determined by thermal analysis (see below). The anhydrous NNT adopts similar sheet-like crystallites (**Table S1** and **S3**). However, the unit cell is significantly contracted; in particular, the *c* parameter is 12% smaller than it is for the as-prepared material. This contracted *c* axis occurs due to a decrease in interlayer spacing consistent with the loss of water from the interlayer space to form $NaTi_3O_6OH$. Interestingly, in addition to the loss of water and corresponding interlayer contraction, there is also a rearrangement of the sodium ions in the interlayer space (**Fig. S2b**). The decrease in the interlayer spacing and the loss of water from the sodium's coordination sphere causes the formation of O-Na-O bridges between the titania layers. The existence of these bridges was previously suspected based on IR and Raman spectroscopy results.[15]

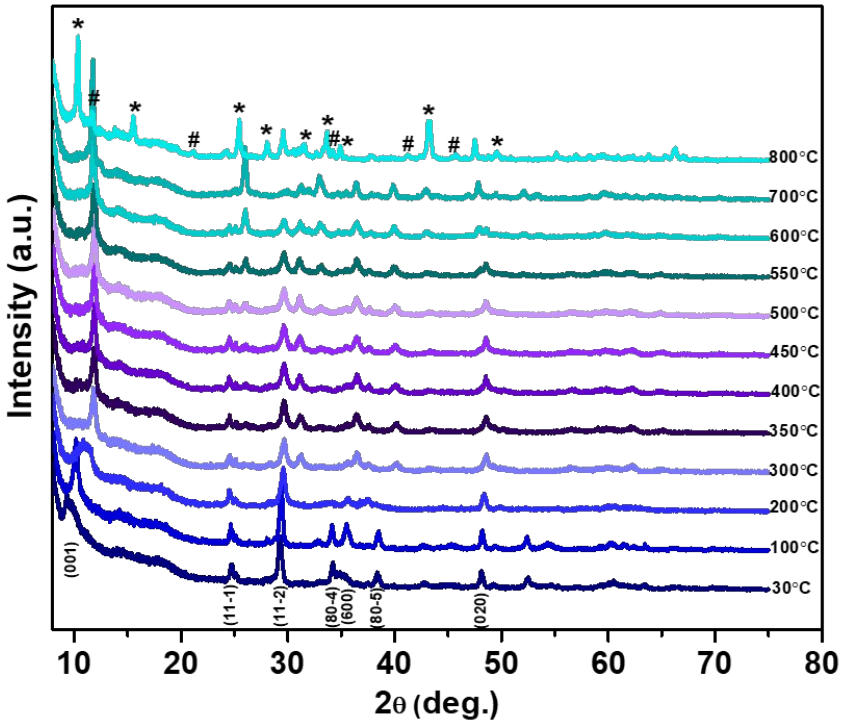


**Fig 2.** Temperature-controlled XRD patterns of as-synthesized NNT under argon collected *via* Cu Kα source. (*: $Na_2Ti_3O_7$, #: $Na_2Ti_6O_{13}$)

In our previous NNT study, temperature-controlled XRD revealed structural changes as the temperature increased.[16] It is known that NNT is sensitive to details of the synthesis and washing procedure which affect structure.[15] Therefore, further investigation to determine the optimal dehydration temperature of NNT is required. **Fig. 2** shows a series of XRD patterns

collected every 50 ˚C until the NNT decomposes to $Na_2Ti_3O_7$ and $Na_2Ti_6O_{13}$ at 800 ˚C. Below 100˚C there are no significant changes in the XRD pattern, and a slight mass loss is shown in the TGA analysis (**Fig. S3**), indicating loss of physisorbed water. At 200 ˚C, the (001) and (11-2) reflections broaden considerably due to the presence of a second partially dehydrated phase. Beginning at 300 ˚C the (001) peak shifts to a higher 2θ, consistent with further loss of interlayer water. This structural change is captured at an earlier temperature than in our previous study, probably because of some differences in the way the experiment was carried out. From **Fig S3**, there is only a 1% mass loss difference between 300-600 ˚C. This suggests that complete dehydration can be carried out at lower temperatures than the 600 ˚C used in the earlier study, if done for a sufficient length of time. Based on this observation, we decided to investigate the electrochemical behavior of this electrode material after drying at temperatures ranging from 300-800 ˚C.

***Effect of Drying Temperature on NNT Performance***

**Fig. 3** shows the voltage profiles of half-cells containing carbon coated NNTs prepared at various temperatures ranging from 300-800 ˚C, compared to the as-synthesized (hydrous) material without carbon coating. In the first cycle, the as-made material and those heated to moderate temperatures (up to 500 ˚C) deliver specific discharge capacities above 260 mAh/g, but side-reactions including SEI formation contribute to this value. A truer measure of utilization is discharge capacity of these cells during the second cycle, which is more reversible (**Fig. 3b**). With the exception of the material heated to 800 ˚C, the voltage profiles have similar features, but NNT heated to 500 ˚C gives the highest discharge capacity of nearly 200 mAh/g. The first few cycles of cells containing this material are shown in **Fig. 3a-b** and cycling data is shown in **Fig. 3c**. The NNT dehydrated at 500 ˚C retains most of its discharge capacity with a CE of 98.9% after the first cycle. For cells containing materials heated above this temperature, the 2$^{nd}$ cycle discharge capacity is somewhat lower (compare the voltage profiles for the material heated to 500 and 600 ˚C in **Fig. 3b**). A change in the voltage characteristics is apparent for the cell containing the material heated to 800 ˚C, which does not exhibit the multiple small plateaus seen between about 1.2-0.4 V observed in the other cells, but rather a steeply sloping section, followed by a plateau below 0.3 V. This is consistent with the decomposition to $Na_2Ti_3O_7$ and $Na_2Ti_6O_{13}$ seen in **Fig. 2**.[12,14] $Na_2Ti_6O_{13}$ discharges at about 0.9 V vs. $Na^+/Na$ and $Na_2Ti_3O_7$ exhibits a flat discharge profile at around 0.3 V in the same configuration.

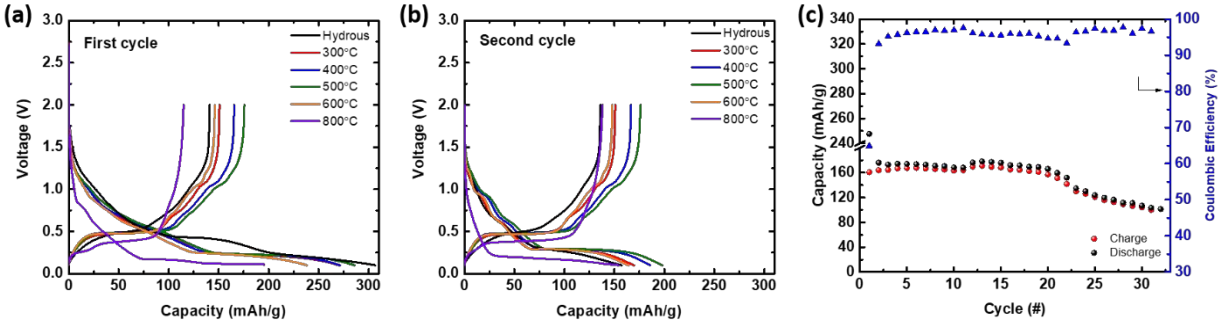


**Fig. 3.** The potential versus specific capacity profile for the NNT samples dehydrated at various temperatures for **(a)** first cycle and **(b)** second cycle in Na half-cells. **(c)** Capacity retention and Coulombic efficiency for the NNT sample dehydrated at 500 ˚C. All electrodes contained CMC binders and the cells were cycled between 2.0 and 0.1 V at 0.15 mA $cm^{-2}$.

The observation of distinct reversible plateaus at ~0.6 V and 1.1 V during the second and subsequent cycles for most of the NNT electrodes in **Fig. 3** correlate well with peaks observed in their cyclic voltammetry profiles shown in **Fig. S4.** These features are less obvious during the first cycle, in the hydrous material, in electrodes made with PVDF rather than CMC (**Fig. S4d**), or at higher cycling rates, because of side reactions (e.g., irreversible sodium insertion into carbon seen in **Fig. S4d**) and kinetic effects. These features occur at somewhat different potentials than those exhibited by related structures such as tunnel-containing $Na_2Ti_6O_{13}$ (discharge at 0.87 V vs. $Na^+/Na$ with a capacity of 65 mAh/g and good reversibility) [12,15] or layered $Na_2Ti_3O_7$ (0.3 V, 200 mAh/g).[14] The results in **Fig. 2** also indicate that dehydrated NNT has excellent thermal stability and that the bulk does not decompose until temperatures above 600 ˚C are reached at the heating rates used for that experiment. These phases were also not detected in the synchrotron XRD pattern of the material dried at 600 ˚C for 2 hours. The discharge profiles of half-cells containing NNT heated to 800 ˚C, which caused it to decompose, also looks quite different, and the cycling behavior is inferior to that of cells containing NNTs treated at lower temperatures (**Fig. S5**). Thus, these features probably do not belong to separate impurity phases resulting from thermal treatment. There are structural changes occurring upon dehydration (**Fig. S2b**) that result in several different environments for sodium ions accounting for the complex discharge profile. In particular, the formation of O-Na-O bridges impart a quasi-tunnel-like structure reminiscent of $Na_2Ti_6O_{13}$, which result in the stable cycling observed in the CV curves (**Fig. S4)**.

### *NNT Electrode Optimization*

The electrochemical properties of NNT reported earlier revealed some limitations resulting in lower than expected capacity and high first cycle inefficiency. This is due in part to the low electronic conductivity of the pristine titanate and the very low voltage at which it operates, which results in side reactions that contribute to the formation of the solid electrolyte interphase (SEI). Following the procedure by S. Lee *et al.*[20], NNT was carbon coated using sucrose pyrolysis to improve the electronic conductivity. **Fig. S6** shows the SEM images of the as-synthesized NNT and carbon coated NNT nanowires, indicating that the procedure did not change the particle

morphology. Both samples consist of an agglomeration of nanowires that range from 100-200 nm in length with varying widths. **Fig. S7** shows TGA of the sucrose-treated sample heated in air, indicating that the carbon content of the sample is about 9.5 wt. %.

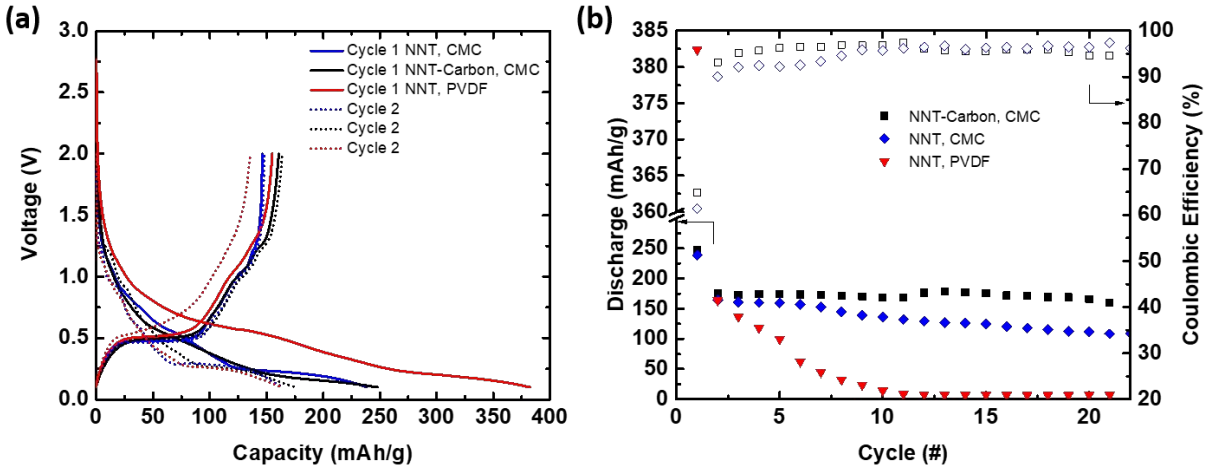


**Fig. 4. (a)** Potential versus specific capacity profile and, **(b)** capacity retention and Coulombic efficiency for NNT samples dehydrated at 500 ˚C with or without carbon coating in Na half-cells, with different binders (CMC or PVDF). All cells were cycled between 2.0 and 0.1 V at 0.15 mA $cm^{-2}$.

For low voltage anodes, finding a compatible binder is critical for obtaining optimum electrochemical performance.[25] The electrochemical performance of anhydrous-NNT can be further improved based on our previous studies, where PVDF was used as the binder in the composite electrodes.[16,19] Carboxymethyl cellulose (CMC) contains -OH and -COOH functional groups that strongly interact with the active material and has been shown to improve the performance of silicon anodes.[19] Based on the silicon anode work[26], CMC was studied as a potential replacement for PVDF. A comparison of performance between electrodes made with PVDF and those with CMC is shown in **Fig. 4.** A change from PVDF to CMC binder resulted in dramatically better capacity retention. The capacity retention was further improved for the electrode that was carbon-coated. Interestingly, changing to a CMC binder also greatly improved the performance of the as-synthesized (hydrous) NNT even without carbon coating (**Fig. S8)**: compare to results reported in reference 16. In that reference, poor cycling was attributed to degradation of the NNT electrode made with PVDF, based on impedance analysis. The improved electrochemical performance of hydrous-NNT with CMC binder is likely due to the strong interactions between the COOH/-OH functional groups and the active material and current collector, which aid in maintaining the electrode integrity as volume changes associated with cycling occur. By optimizing the thermal treatment, improving electronic conductivity by adding carbon, and incorporating CMC binder into the electrodes, it is possible to obtain the theoretical capacity of NNT.

***Graphene-wrapped NNT***

A second method of improving electronic conductivity in NNT composites was also attempted. For this part of the work, graphene-wrapped NNT composites were synthesized hydrothermally using a bottom-up approach. A small amount of graphene oxide was added to precursor mixture prior to the hydrothermal treatment under otherwise identical conditions. Note that GO is probably not fully reduced under the conditions of synthesis, but is expected to undergo irreversible reduction to rGO electrochemically during the first discharge in half cells. To determine the structural influence of the incorporation of graphene oxide (GO) into the NNT structure, synchrotron XRD patterns were collected on the NNT-GO composites and compared to as-prepared NNT and anhydrous-NNT (**Fig. S9)**. The XRD patterns of the as prepared NNT and the anhydrous-NNT are almost identical to their GO containing counterparts suggesting that its incorporation has minimal impact on the resulting NNT structure.

The XRD patterns were refined to obtain more quantitative information and the results and fits are shown in **Table S1** and **Fig. 5,** respectively. The XRD patterns can be effectively fit to the $NaTi_3O_6OH{\cdot}xH_2O$ phase where $x$=2 for the as-prepared graphene-wrapped material, and $x$=0 for the graphene-wrapped anhydrous material with no peaks detected corresponding to any other phases. Very similar to the results for the pristine NNT materials shown in **Table S1**, the unit cell for the as prepared NNT-GO is comparable to the literature values[24] while the anhydrous NNT-GO has a significant $c$ axis contraction and, like the parent compounds, both materials are comprised of sheet-like crystallites. Furthermore, the refinements show O-Na-O bridges connecting the titania layers in the anhydrous NNT-GO material similar to anhydrous-NNT (**Fig. S2b**). As there are no significant structural differences between the NNT-GO materials and their pristine NNT analogs and no additional peaks are observed in the XRD patterns, the NNT-GO materials can best be described as graphene-wrapped NNT composites where amorphous GO is intimately mixed with the NNT nanoparticles, rather than being present in the interlayer spaces. The amount of graphene in the NNT-GO composites was determined to be 1 wt.% by TGA analysis in air (**Fig. S10a**). SEM images also indicate that NNT-GO composites have similar nanowire like morphology as graphene-free NNT samples (**Fig. S10b**).

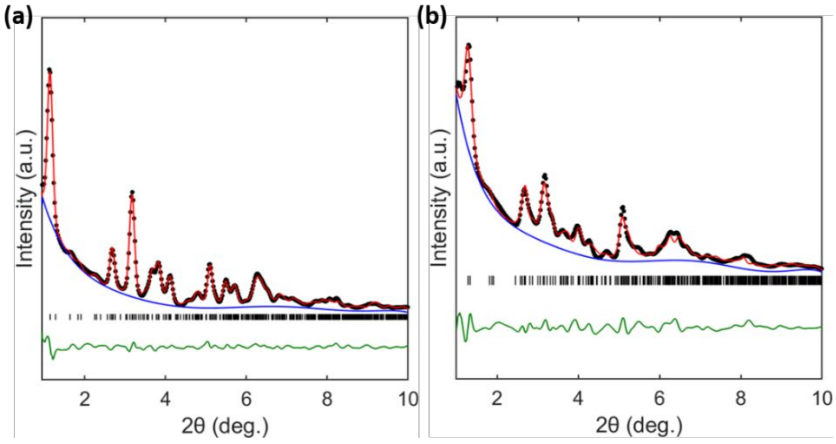


**Fig. 5.** Rietveld refinements of XRD patterns of **(a)** NNT-GO as-prepared (%$R_{wp}$=2.82) and **(b)** anhydrous NNT-GO (%$R_{wp}$=3.55). The black points represent the data, the red line represents the

fit, the blue is the background, and the green is the difference between the experimental data and the fit. The black lines represent the expected reflections from the structural model.[24]

To corroborate the structural information gained from the XRD analysis, pair distribution functions (PDF) were obtained for both graphene-wrapped and graphene-free as-prepared NNT and anhydrous NNT (**Fig. 6**). The first four peaks in the PDF are observed at 1.97, 2.58, 3.15, and 3.72 Å for both types of materials; this is consistent with the structural models determined through Rietveld refinement. The peaks correspond to the titanium-oxygen bonding distance, the sodium-oxygen bonding distance, the titanium-titanium distance, and the 2nd titanium-titanium and titanium-oxygen distances respectively. Past ~7 Å, differences can be observed in the PDF of the as-prepared NNT and the anhydrous NNT. This is consistent with the XRD results as both structures have similar short-range order, while their longer-range order is different due to the differences in how the $TiO_6$ layers stack. The PDF data was fit according to the structural models determined from the XRD analysis (**Fig. 6**). The PDF data validates the observations made from the XRD patterns that indicate that both materials are layered, with a smaller interlayer spacing and O-Na-O bridges in the case of the anhydrous material. Materials with and without graphene oxide have very similar PDF patterns as the parent materials, giving further evidence of the presence of GO on particle surfaces, rather than between the titanate layers, which would change the crystal structure of the material.

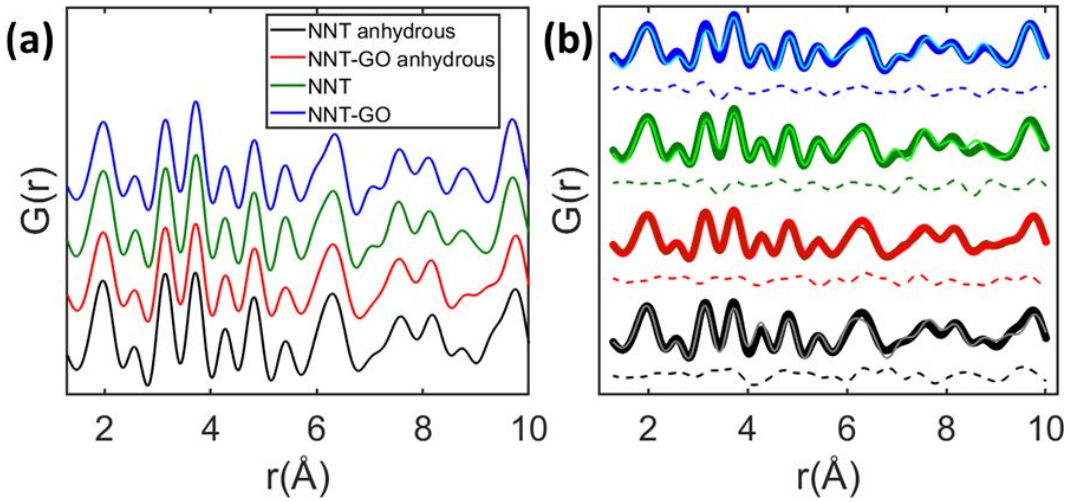


**Fig. 6. (a)** PDF's of as-prepared NNT and anhydrous NNT (annealed at 600 °C) with and without graphene (GO) wrapping. **(b)** PDF fits to the $NaTi_3O_6OH{\cdot}xH_2O$ models used for the XRD patterns. Anhydrous NNT is shown in black ($\%R_{wp}$=31.0), anhydrous NNT-GO is red ($\%R_{wp}$=26.1), NNT is green ($\%R_{wp}$=29.6), and NNT-GO is blue ($\%R_{wp}$=26.1).

The electrochemical performance of graphene-wrapped NNT samples heated to 500 ˚C, using either PVDF or CMC binder in sodium half-cell configurations is presented in **Fig. S11 and**

**S12**. Interestingly, capacity retention for the graphene-wrapped NNT made with PVDF binder is excellent, although the full capacity is not obtained at moderate current densities. Better results are found when a CMC binder is used, with about 170 mAh/g delivered on the second discharge at the same rate. This suggests that graphene-wrapping may also be an effective way to improve electronic conductivity for this system, particularly since very little needs to be used to see significant improvement.

### *Mechanistic Understanding of NNT by Synchrotron X-ray Absorption Spectroscopy (XAS)*

#### *Hard and Soft XAS analysis NNT*

Synchrotron X-ray absorption spectroscopy (XAS) was used to obtain further insights on the redox properties of anhydrous NNT. Hard X-ray absorption near edge spectroscopy (XANES) yields information on the bulk material changes regarding the electronic structure and transition metal local environments.[27] The core electrons that have a stronger bond to the nucleus requiring higher photon energies for photoionization, which lead to higher oxidation states. A shift to lower energy indicates a lower oxidation state for the transition metal being probed. **Fig. 7** shows the changes of the Ti XANES energies as a function of state of charge (SoC), using edge positions at 50% intensity values. In the pristine material the Ti oxidation state is 4+ with an edge position of 4947 eV. As NNT is discharged to 0.1V, the Ti edge position shifts to a lower energy indicting that Ti has been reduced.[28] The edge position for the fully discharged electrode is close to the reference spectra of $Ti_2O_3$ ($Ti^{3+}$). The pre-edge peaks also contain information about metal coordination and provides further evidence for the reduction to $Ti^{3+}$ during discharge. The three peaks labeled A1-A3 are due to the Ti 1s-core electrodes transitioning to the unoccupied Ti 3d-4s/4p hybridized states.[29] The A1 peak is due to the $t_{2g}$ bonding states while A2 is the nondirectional $e_g$ antibonding states. The A3 peak has more 4p character and is hybridized with Ti-4s and possibly the O-2p orbital. For the discharged electrodes, the A1 and A2 peak intensity decreases due to sodium insertion.

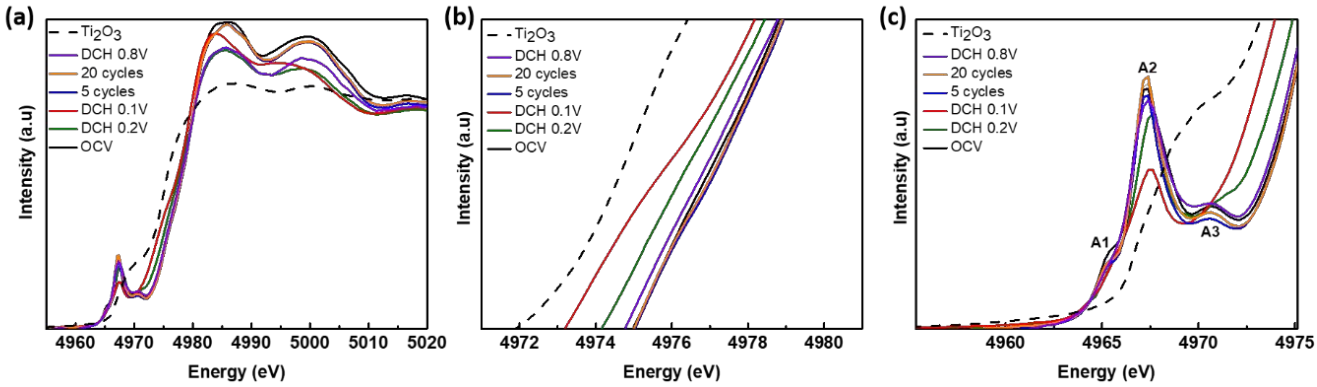


**Fig. 7.** X-ray absorption spectroscopy XANES measurements of the Ti K-edge in the pristine state and cycled at various states of charge.

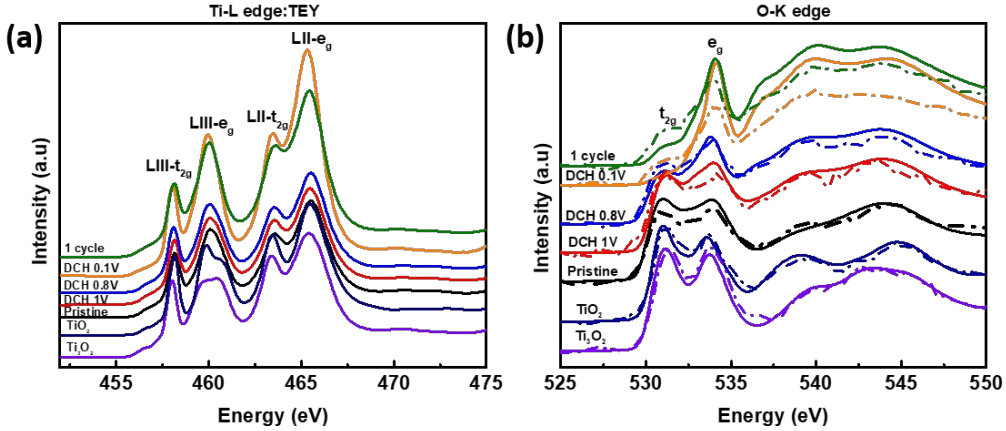


**Fig. 8.** Soft X-ray absorption spectroscopy measurements of **(a)** the TEY Ti L-edge, and **(b)** O K-edge in the TEY (solid line) and FY (dotted line) modes. The measurements are compared to standards and obtained on NNT electrodes discharged and charged to the indicated states-of-charge. Soft XAS spectra for $TiO_2$ and $Ti_2O_3$ reference materials are also included.

While hard XAS probes the transition metal K-edge in the bulk of the material, soft XAS probes the L-edge in the sub-surface regions of the material, with the depth dependent on the detection mode. The fluorescence yield (FY) mode penetrates approximately 100 nm into the sample, and total electron yield (TEY) mode about 5-10 nm in. Soft XAS investigates the dipole allowed electron excitations stemming from 2p to 3d; this includes the $2p_{3/2}$ ($L_{III}$) and $2p_{1/2}$ ($L_{II}$) spin orbit states.[30,31] The fingerprints for valence state, spin state, and chemical bonding states are caused by specific element excitations.

**Fig. 8a** compares the NNT electrodes cycled to different states-of-charge to those of the reference samples ($TiO_2$ ($Ti^{4+}$) and $Ti_2O_3$ ($Ti^{3+}$)). TEY mode (5-10nm in) gives information on the Ti redox state near the surface. The $L_{III}$ and $L_{II}$ peaks are due to the Ti $2p_{3/2}$ and $2p_{1/2}$ and core transitions to unoccupied stated (Ti $3d_{5/2}$ and Ti $3d_{3/2}$); these are split into the $t_{2g}$ and $e_g$ states.[32] Focusing on the $L_{III\text{-}t2g}$ peak, the peak position of the pristine NNT is at the same position as the $TiO_2$ reference, indicating a $Ti^{4+}$ oxidation state. This peak shifts to a lower energy for the electrode discharged to 0.1 V; aligning more with the $Ti^{3+}$ reference. During discharge, the $TiO_6$ octahedra become distorted as evidence by the $L_{III\text{-}eg}$ peak widening, due to the Jahn-Teller effect. A similar phenomena occurs during the lithiation of $TiO_2$, as observed by Guo *et al*.[33]

**Fig. 8b** shows the oxygen K-edge XAS spectra, which contains two regions. The first, corresponds to the local intensity maxima between 528-535 eV and is related to the O 1s transition to TM3d-O2p hybridized states, the second, is the high energy region above 535 eV corresponding to the O 1s transitions to hybridized TM 4sp-O2p states. For NNT discharged to 0.1 V, the $t_{2g}$ peak decreases while the $e_g$ peak increases. This happens in both FY (100 nm depth) and TEY modes. The trends observed at the Ti L-edge are consistent with those seen in the O K edge. However,

after the first cycle, the TM3d-Op region did not fully recover to the pristine state, indicating that not all of the titanium is re-oxidized to the tetravalent state. This apparent irreversibility is also observed for cycled electrodes in the XANES Ti-K-edge data.

These results are consistent with a classical reversible reductive intercalation mechanism for NNT electrodes rather than pseudocapacitance. This is supported by limited *ex situ* XRD results on discharged electrodes, which show changes consistent with insertion of sodium ions between the titanate layers,[19] and also by a color-change from white to deep blue, characteristic of trivalent titanium, in carbon-free electrodes that have been discharged (see optical images shown in **Fig. S13**). Full reduction of all titanium in NNT to the trivalent state would result in a theoretical capacity of over 300 mAh/g, but site limitations prevent this from happening reversibly. Based on these structural considerations, a reversible capacity of about 200 mAh/g is expected, and full utilization can be achieved through material and structural engineering.

## Conclusions

A structural examination of as-synthesized and dehydrated NNT using synchrotron X-ray diffraction and pair distribution function analyses shows that there is a 12% decrease in the interlayer spacing upon drying and rearrangement of sodium ions to form O-Na-O bridges. No significant structural changes were observed for composites made with graphene oxide, suggesting that it is located on particle surfaces rather than in the interlayer spacings. Both carbon-coating via a sucrose pyrolysis method or graphene-wrapping resulted in better electrochemical properties for NNT, presumably because of improved electronic conductivity. Hard and soft XAS experiments on pristine, discharged, and cycled electrodes show results consistent with reduction of tetravalent titanium to the trivalent state during discharge, although the process is not entirely reversible. This is consistent with a classical reversible reductive intercalation mechanism. The optimum dehydration temperature was found to be 500 ˚C based on a comparison of the discharge properties. Further improvements in the cycling behavior were obtained by changing to a CMC binder, which can more readily accommodate volume changes associated with NNT redox processes than PVDF. By combining these strategies, it was possible to obtain a 2$^{nd}$ discharge capacity of 200 mAh/g, corresponding to 100% utilization of the electrode, with good capacity retention upon cycling and a high Coulombic efficiency after the first cycle.

## Acknowledgements

This work was supported by the Assistant Secretary for Energy, Efficiency and Renewable Energy, Office of Vehicle Technologies of the U.S. Department of Energy under Contract No. DE-AC02-05CH11231.

Work at the Molecular Foundry of Lawrence Berkeley National Lab (LBNL) was supported by the Office of Science, Office of Basic Energy Sciences of the U.S. Department of Energy under Contract No. DE-AC02-05CH11231. We would like to acknowledge the use of the Stanford Synchrotron Radiation Lightsource, SLAC National Accelerator Laboratory, that is

supported by the U.S. Department of Energy, Office of Science, Office of Basic Energy Sciences under Contract No. DE-AC02-76SF00515. This work was also supported as part of the Center for Mesoscale Transport Properties, an Energy Frontier Research Center supported by the U.S. Department of Energy, Office of Science, Basic Energy Sciences, under award #DE-SC0012673. The X-ray diffraction data was collected on beamline 28-ID-1 of the National Synchrotron Light Source II, a U.S. Department of Energy (DOE) Office of Science User Facility operated for the DOE Office of Science by Brookhaven National Laboratory under Contract No. DE-SC0012704. E.S.T. acknowledges support as the William and Jane Knapp Chair of Energy and the Environment.



**Corresponding Author**

*E-mail: mmdoeff@lbl.gov

**Author Contributions**

§ These authors contributed equally to this work.

## References


[1] G. Hasegawa, K. Kanamori, N. Kannari, J. Ozaki, K. Nakanishi and T. Abe, *ChemElectroChem*, 2015, **2**, 1917–1920.

[2] S. Komaba, W. Murata, T. Ishikawa, N. Yabuuchi, T. Ozeki, T. Nakayama, A. Ogata, K. Gotoh and K. Fujiwara, *Adv. Funct. Mater.*, 2011, **21**, 3859–3867.

[3] Y. Li, Y. S. Hu, M. M. Titirici, L. Chen and X. Huang, *Adv. Energy Mater.*, 2016, **6**, 1600659.

[4] Z. Li, Z. Jian, X. Wang, I. A. Rodrı´guez-Pe´rez, C. Bommier and X. Ji, *Chem. Commun.*, 2017, **53**, 2610–2613.

[5] S. Komaba, T. Ishikawa, N. Yabuuchi, W. Murata, A. Ito and Y. Ohsawa, *ACS Appl. Mater. Interfaces*, 2011, **3**, 4165–4168.

[6] M. Dahbi, T. Nakano, N. Yabuuchi, S. Fujimura, K. Chihara, K. Kubota, J. Y. Son, Y. T. Cui, H. Oji and S. Komaba, *ChemElectroChem*, 2016, **3**, 1856–1867.

[7] M. Lao, Y. Zhang, W. Luo, Q. Yan, W. Sun and S. X. Dou, *Adv. Mater.*, 2017, **29**, 1700622.

[8] B. Farbod, K. Cui, W. P. Kalisvaart, M. Kupsta, B. Zahiri, A. Kohandehghan, E. M. Lotfabad, Z. Li, E. J. Luber and D. Mitlin, *ACS Nano*, 2014, **8**, 4415–4429.

[9] W. J. Li, S. L. Chou, J. Z. Wang, H. K. Liu and S. X. Dou, *Chem. Commun.*, 2015, **51**, 3682–3685.

[10] J. Mao, X. Fan, C. Luo and C. Wang, *ACS Appl. Mater. Interfaces*, 2016, **8**, 7147–7155.

[11] L. Wu, F. Pei, R. Mao, F. Wu, Y. Wu, J. Qian, Y. Cao, X. Ai and H. Yang, *Electrochim. Acta*, 2013, **87**, 41–45.

[12] A. Rudola, K. Saravanan, S. Devaraj, H. Gong and P. Balaya, *Chem. Commun.*, 2013, **49**, 7451-7453.

[13] H. Pan, X. Lu, X. Yu, Y. S. Hu, H. Li, X. Q. Yang and L. Chen, *Adv. Energy Mater.*, 2013, **3**, 1186–1194.

[14] P. Senguttuvan, G. Rousse, V. Seznec, J. M. Tarascon and M. R. Palacin, *Chem. Mater.*, 2011, **23**, 4109–4111.

[15] M. M. Doeff, J. Cabana, and M. Shirpour, *J. Inorg. Organomet. Polym. Mater.*, 2014, **24**, 5–14.

[16] M. Shirpour, J. Cabana and M. M. Doeff, *Energy Environ. Sci.*, 2013, **6**, 2538-2547.

[17] M. Shirpour, J. Cabana and M. M. Doeff, *Chem. Mater.*, 2014, 26, **8**, 2502–2512.

[18] I. M. Markus, S. Engelke, M. Shirpour, M. Asta and M. M. Doeff, *Chem. Mater.*, 2016, **28**, 4284–4291.

[19] D. Seshadri, M. Shirpour and M. M. Doeff, *J. Electrochem. Soc.*, 2015, **162**, A52–A59.

[20] S. Lee, Y. Cho, H. K. Song, K. T. Lee and J. Cho, *Angew. Chemie - Int. Ed.*, 2012, **51**,

8748–8752.

[21] B. H. Toby and R. B. Von Dreele, *J. Appl. Crystallogr.*, 2013, **46**, 544–549.

[22] X. Yang, P. Juhas, C. L. Farrow and S. J. L. Billinge, *arXiv Prepr. arXiv1402.3163*, 2014.

[23] C. L. Farrow, P. Juhas, J.W. Liu, D. Bryndin, E.S. Božin, J. Bloch, T. Proffen and S. J. Billinge, *J. Phys. Condens. Matter*, 2007, **19**, 335219.

[24] I. Andrusenko, E. Mugnaioli, T. E. Gorelik, D. Koll, M. Panthöfer, W. Tremel and U. Kolb *Acta Crystallogr. Sect. B Struct. Sci.*, 2011, **67**, 218–225.

[25] H. Shobukawa, J. Alvarado, Y. Yang and Y. S. Meng, "*J. Power Sources*, 2017, **359**, 173–181.

[26] C. C. Nguyen, T. Yoon, D. M. Seo, P. Guduru and B. L. *ACS Appl. Mater. Interfaces* 2016, **8**, 12211–12220.

[27] H. Shobukawa, J. Shin, J. Alvarado, C. S. Rustomji and Y. S. Meng, *J. Mater. Chem. A*, 2016, **4**, 15117–15125.

[28] J. Alvarado, C. Wei, D. Nordlund, T. Kroll, D. Sokaras, Y. Tian, Y. Liu and M. M. Doeff, *Mater. Today*, 2020, **35**, 87-98.

[29] J. Xu, C. Ma, M. Balasubramanian and Y. S. Meng, *Chem. Commun.*, 2014, **50**, 12564–12567**.**

[30] X. Yu, H. Pan, W. Wan, C. Ma, J. Bai, Q. Meng, S. N. Ehrlich, Y. S. Hu, X. Q. Yang and X. Yu, *Nano Lett.*, 2013, **13**, 4721–4727.

[31] F. Lin, Y. Liu, X. Yu, L. Cheng, A. Singer, O. G. Shpyrko, H. L. Xin, N. Tamura, C. Tian, T. C. Weng and X. Q. Yang, *Chem Rev*. 2017, **8**, 13123-13186.

[32] F. Lin, D. Nordlund, Y. Li, M. K. Quan, L. Cheng, T. C. Weng, Y. Liu, H. L. Xin and M. M. Doeff, *Nat. Energy*, 2015, **1**, 15004.

[33] Y. Ye, M. Kapilashrami, C. H. Chuang, Y. S. Liu, P. A. Glans and J. Guo, *MRS Commun.*, 2017, **7**, 53–66.

[34] J. Guo, *Int. J. Quantum Chem.*, 2009, **109**, 2714-2721.

**TOC Graphic**

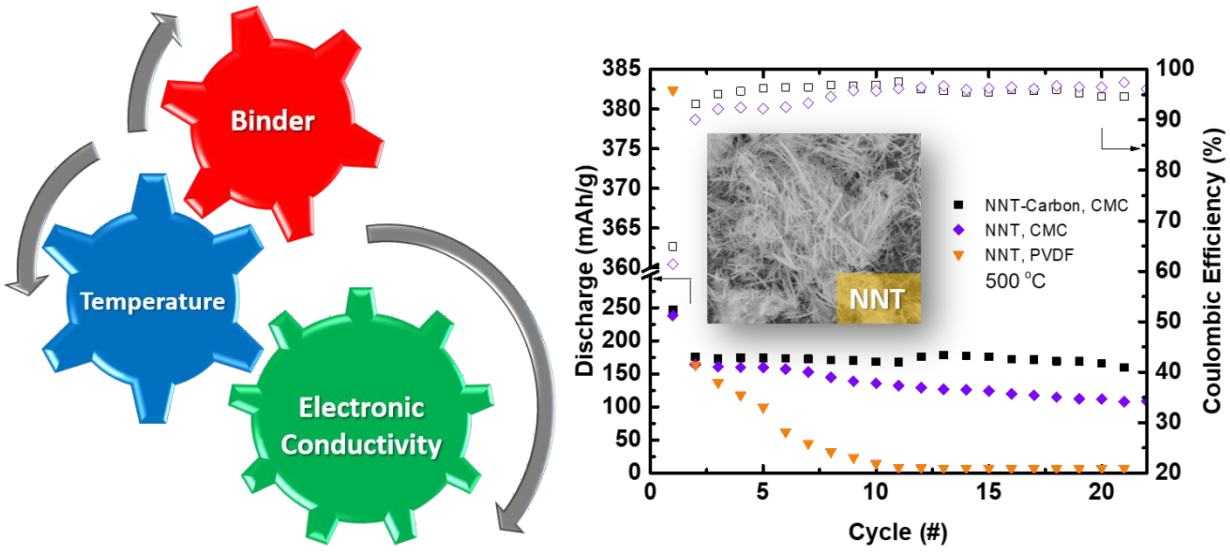
Binder
Temperature
Electronic Conductivity
Discharge (mAh/g)
Coulombic Efficiency (%)
Cycle (#)
NNT
NNT-Carbon, CMC
NNT, CMC
NNT, PVDF
500 °C